HHS Public Access

Author manuscript

*ACS Nano*. Author manuscript; available in PMC 2017 January 06.

Published in final edited form as:

*ACS Nano*. 2016 January 26; 10(1): 1355–1362. doi:10.1021/acsnano.5b06759.

# Ultrahigh $^{19}F$ Loaded $Cu_{1.75}S$ Nanoprobes for Simultaneous $^{19}F$ Magnetic Resonance Imaging and Photothermal Therapy

**Hongli Chen**[†,⊥], **Manli Song**[‡,⊥], **Juan Tang**[†,⊥], **Gaofei Hu**[†], **Suying Xu**[†], **Zhide Guo**[‡], **Nannan Li**[†], **Jiabin Cui**[†], **Xianzhong Zhang**[*,‡], **Xiaoyuan Chen**[*,§], and **Leyu Wang**[*,†]

[†]State Key Laboratory of Chemical Resource Engineering, Beijing University of Chemical Technology, Beijing 100029, People's Republic of China

[‡]Center for Molecular Imaging and Translational Medicine, State Key Laboratory of Molecular Vaccinology and Molecular Diagnostics, School of Public Health, Xiamen University, Xiamen, Fujian 361005, People's Republic of China

[§]Laboratory of Molecular Imaging and Nanomedicine (LOMIN), National Institute of Biomedical Imaging and Bioengineering (NIBIB), National Institutes of Health (NIH), Bethesda, Maryland 20892, United States

## Abstract

$^{19}F$ magnetic resonance imaging (MRI) is a powerful noninvasive, sensitive, and accurate molecular imaging technique for early diagnosis of diseases. The major challenge of $^{19}F$ MRI is signal attenuation caused by the reduced solubility of probes with increased number of fluorine atoms and the restriction of molecular mobility. Herein, we present a versatile one-pot strategy for the fabrication of a multifunctional nanoprobe with high $^{19}F$ loading (~$2.0 \times 10^8$ $^{19}F$ atoms per $Cu_{1.75}S$ nanoparticle). Due to the high $^{19}F$ loading and good molecular mobility that results from the small particle size (20.8 ± 2.0 nm) and ultrathin polymer coating, this nanoprobe demonstrates ultrahigh $^{19}F$ MRI signal. *In vivo* tests show that this multifunctional nanoprobe is suitable for $^{19}F$ MRI and photothermal therapy. This versatile fabrication strategy has also been readily extended to other single-particle nanoprobes for ablation and sensitive multimodal imaging.

## Graphical Abstract

[*]Corresponding Authors: zhangxzh@xmu.edu.cn, shawn.chen@nih.gov, lywang@mail.buct.edu.cn.

[⊥]**Author Contributions**

H.C., M.S., and J.T. contributed equally.

The authors declare no competing financial interest.

Supporting Information

The Supporting Information is available free of charge on the ACS Publications website at DOI: 10.1021/acsnano.5b06759.

Rough calculation of $^{19}F$ atoms on the nanoprobe surface, XRD pattern (Figure S1), TEM images and cytotoxicity tests of $Cu_{1.75}S$–$^{19}F$@OFP–thiol-PEG NPs (Figure S2), TEM images and cytotoxicity tests of $Cu_{1.75}S$–$^{19}F$@OFP–PVP NPs (Figure S3), TEM images of $Cu_{1.75}S$@OFP NPs and $Cu_{1.75}S$–$^{19}F$@OFP NPs prepared with different amount of NaOH solution (Figure S4), TEM images of $Cu_{1.75}S$–$^{19}F$@OFP NPs prepared with various amounts of PFCE and calibration curve for $^{19}F$ quantitation (Figure S5), photothermal images and temperature evolution profiles (Figure S6), evolution plots of the tumor size (a) and the body weight (b) of mice in control experiments (Figure S7), and UV–vis–NIR absorption spectrum (Figure S8) (PDF)

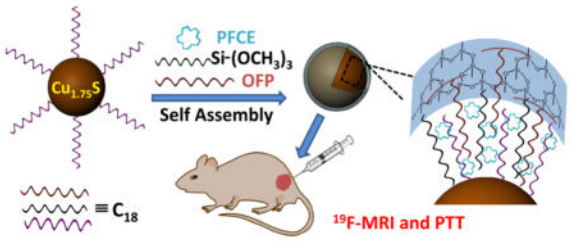


**Keywords**

$^{19}$F MRI; photothermal imaging and therapy; multifunctional nanoprobes; copper sulfide nanoparticle

Among many *in vivo* imaging modalities, magnetic resonance imaging (MRI) is advantageous because it is noninvasive and can provide valuable information about deep tissues in living subjects with high spatial resolution without using radioactivity.[1,2] $^{19}$F MRI is anticipated to be a promising alternative to conventional $^{1}$H MRI because of its high sensitivity (0.83 relative to $^{1}$H),[3–6] negligible background signals,[7] and cost-effectiveness, which allows direct detection of $^{19}$F-labeled probes such as cells[6,8] and drug capsules[9] for unambiguous identification and quantification, unlike typical metal-based contrast agents.[10,11] In order to obtain highly sensitive $^{19}$F MRI probes for their practical implications, it is important to increase the number of fluorine atoms in the MRI probes. Owing to the large number of fluorine atoms, current $^{19}$F MRI contrast agents focus on perfluoropolyether (PFPE) in either linear or macrocyclic structures. Unfortunately, the split multiple fluorine signals of linear PFPE may result in low signal intensity and imaging artifacts. In the case of macrocyclic PFPE, the fluorophilic feature makes it insoluble in most solvents. Besides, increasing number of fluorine atoms would result in larger molecular size as well as higher restriction of molecular mobility, which, in turn, causes attenuation of the $^{19}$F MRI signal.[10,12,13] PFPE has been successfully encapsulated in nanoemulsion as a $^{19}$F MRI contrast agent for *in vivo* imaging.[6,14–17] However, the performance of these nanoemulsions is dramatically impaired due to their poor stability, which originates from the molecular diffusion induced particle size expansion. To overcome this limitation, Kikuchi's group reported a multifunctional $^{19}$F MRI nanoprobe with an average size of 76 ± 9 nm by coating the nanoemulsion with a silica shell.[12] Another strategy to increase the fluorine content in the probe while maintaining high segmental molecular mobility is to fabricate supramolecular or polymer $^{19}$F nanoprobes.[2,18,19]

In addition, dual-modality probes with a high number of fluorine atoms have also been explored in the past decades.[20–23] A facile and robust method has been proposed by loading the fluorous dendron tethered with a near-infrared (NIR) cyanine dye (F27-Cy5.5) into a polymeric nanoparticle with an average size of 130 nm for simultaneous $^{19}$F MR imaging and NIR fluorescence imaging.[24] The $^{19}$F polymeric nanoparticles modified with fluorescent dyes were also used for MRI-optical multimodal imaging.[25,26] By attaching the perfluorocarbon (PFC) onto quantum dots and then fabricating into a magneto-fluorescent nanocomposite emulsion with size of 290 nm, $^{19}$F MRI and fluorescence dual-modality imaging nanoprobe was achieved.[27] Despite the effort, it is still a great challenge to

synthesize single-particle multifunctional nanoprobes with high fluorine content, strong $^{19}F$ MRI signal, small dynamic light scattering (DLS) particle size, good stability, and biocompatibility.

Development of multifunctional platforms for theranostics such as imaging-guided photothermal therapy (PTT) is very active and has attracted much attention in recent years.[28–30] Herein, we have rationally designed a multifunctional $Cu_{1.75}S$–$^{19}F$@OFP–$SiO_2$ nanoprobe with an average size of 20.8 ± 2.0 nm (DLS), which contains up to ~$2.0 \times 10^8$ fluorine atoms per particle with ultrahigh $^{19}F$ MRI signal for simultaneous $^{19}F$ MRI, photothermal imaging (PTI), and PTT. Briefly, the perfluoro-15-crown-5-ether (PFCE) was anchored to the $Cu_{1.75}S$ nanoparticles (NPs)[31–33] through a one-pot encapsulation method by utilizing oleylamine-functionalized polysuccinimide (OFP) and trimethoxy(octadecyl)silane (TMOS) as coencapsulation agents, where the PFCE was anchored through hydrophobic–hydrophobic interactions and then trapped within the silica shell (Scheme 1). These $Cu_{1.75}S$–$^{19}F$@OFP–$SiO_2$ nanoprobes are highly stable, biocompatible, and capable of both *in vivo* imaging ($^{19}F$ MRI and PTI) and photothermal ablation.

## RESULTS AND DISCUSSION

### TEM and DLS Characterization of Nanoprobes

As shown in the transmission electron microscopy (TEM) image (Figure 1a), the as-prepared hydrophobic $Cu_{1.75}S$ NPs, whose crystal structure is confirmed by X-ray diffraction (XRD) (Figure S1), demonstrate uniform shape with an average DLS size of 15.1 ± 1.5 nm (Figure 1b). After being coencapsulated with PFCE using OFP, the $Cu_{1.75}S$–$^{19}F$@OFP nanoprobes are well-dispersed with an average DLS diameter of 21.0 ± 1.9 nm (Figure 1c,d). Compared with the hydrophobic $Cu_{1.75}S$ NPs without surface functionalization, these $Cu_{1.75}S$–$^{19}F$@OFP nanoprobes are stable in water (insets of Figure 1d,f) and the slight increase in the particle size can be attributed to the coating shell. To avoid leakage of PFCE from nanoprobes, an ultrathin $SiO_2$ shell was introduced by hydrolysis of TMOS, which has no observable effects on the particle shape and size (Figure 1e,f) compared with that of $Cu_{1.75}S$–$^{19}F$@OFP (Figure 1c,d).

### FTIR, MRI, and Photothermal Efficiency Characterization of Nanoprobes

The encapsulation of PFCE and silica coating has been characterized *via* Fourier transform infrared (FTIR) spectroscopy (Figure 2a,b). The bands at 1175, 1200, and 1025 $cm^{-1}$ correspond to the C–F, C–O, and Si–O bond vibrations, respectively, indicating the successful fabrication of $Cu_{1.75}S$–$^{19}F$@OFP–$SiO_2$ nanoprobes. Additionally, the $^{19}F$ moieties were confirmed by a $^{19}F$ NMR spectrum with a single peak at −91.85 ppm (Figure 2c) and a half peak width of ~25 Hz that is narrow enough for MRI applications.[6] The preliminary $^{19}F$ MRI results indicated that stronger signals were observed along with the increase of nanoprobe concentration (Figure 2d). The photothermal profile (Figure 2e) illustrated superior thermal effects of the nanoprobe in aqueous medium under the irradiation of a NIR laser (808 nm). The photothermal conversion efficiency ($\eta$) was

calculated to be 54.13% (Figure 2e) according to the reported method,[32,34] which is comparable to or even higher than most of the reported photothermal agents.[35–42]

## Optimization of the Nanoprobe Fabrication Method

For biomedical applications, the biocompatibility of nanoprobes is of crucial importance. Various approaches have been attempted to improve biocompatibility as well as colloidal stability of our material. Thiolated polyethylene glycol (thiol-PEG), which is frequently used for modification of NPs, was first explored. It was found that monodispersed $Cu_{1.75}S$–$^{19}F$@OFP–thiol-PEG NPs could be successfully afforded; yet, the as-prepared NPs were rather cytotoxic (Figure S2). Then, polyvinylpyrrolidone (PVP) was used as a surface ligand to fabricate the $Cu_{1.75}S$–$^{19}F$@OFP–PVP NPs. Compared with $Cu_{1.75}S$–$^{19}F$@OFP–thiol-PEG NPs, the biocompatibility of $Cu_{1.75}S$–$^{19}F$@OFP–PVP NPs was somewhat improved (Figure S3) but still not satisfactory. We presumed that the exposure of nanoparticle surface and thus the leakage of PFCE may account for the cytotoxicity. Therefore, we decided to wrap the nanoparticles with a thin $SiO_2$ shell, which, on the one hand, would maintain the hydrophilic properties of the probes and, on the other hand, anchors the PFCE on the NPs. The $Cu_{1.75}S$–$^{19}F$@OFP–$SiO_2$ NPs with a $SiO_2$ shell of different thicknesses were prepared, and the TEM images indicated that all the nanoprobes were well-dispersed in water (Figure 3a–c). As expected, the biocompatibility of the nanoprobes was significantly improved after the introduction of $SiO_2$ coating. Over 90% of the cells remained alive even after incubation with the nanoprobe as concentrated as 400 $\mu$g/mL (Figure 3d). All the nanoprobes were purified *via* dialysis and centrifugation before cytotoxicity tests and bioapplications.

In addition, little difference on the cytotoxicity of the nanoprobes with $SiO_2$ shells of different thicknesses was observed. Nevertheless, the $^{19}F$ NMR signals decreased with a thicker silica shell (Figure 3e). It is reasonable since the NMR signals are attenuated as the $SiO_2$ shell gets thicker, which limits the mobility of the encapsulated $^{19}F$ moieties.[10,12] Prior to the bioapplications, we also carried out the $^{19}F$ leakage test by dialysis in phosphate buffer solution (PBS, pH 7.4) at room temperature. As shown in Figure 3f, if the nanoprobes were encapsulated with a thin layer of silica *via* the hydrolysis of TMOS (25 $\mu$L), <20% of PFCE on the nanoprobes was released within 12 h. During the next 36 h, no obvious leakage was observed. This leakage can be attributed to the release of PFCE absorbed on the outer face of nanoprobes. Therefore, the dialysis is necessary before bioapplications of these nanoprobes. In the absence of TMOS, about 40% of the PFCE was released from the nanoprobes without silica coating within 12 h. Unlike the silica-coated nanoprobes, a continuous PFCE leakage from the nanoprobes without silica coating was observed even after 48 h. All of the results further indicated that the silica coating is crucial to prevent the PFCE leakage and thus reduce the cytotoxicity as well as maintain the strong MRI signal.

Meanwhile, the preparation procedures were optimized by investigating the impact of different factors. Interestingly, it was found that the introduction of PFCE would affect the phase transfer process. In the absence of PFCE, the dosage of NaOH (0.1 M) in the range of 0.4–1.0 mL has no obvious influence on the particle size and shape (Figure S4). However, in the presence of PFCE, the $Cu_{1.75}S$–$^{19}F$@OFP NPs will aggregate if the NaOH is less than

1.0 mL. In another aspect, the MR signals are linearly correlated with PFCE dosage, yet such enhancement would meet its limit when the dosage is over 15 $\mu$L (Figure S5). Hence, a total volume of 15 $\mu$L of PFCE was used for nanoprobe fabrication. It is noted that the fluorine concentration ($C_F$) was calculated by an external standard method, where $CF_3COONa$ was used as a standard compound, and the calibration curve was plotted by using $C_F$ against the integration area of the MR signal.

To ensure that such an amount of PFCE was enough for $^{19}F$ MR imaging, phantom studies were performed. As shown in Figure 4, very strong $^{19}F$ MRI signals were observed from $Cu_{1.75}S$–$^{19}F$@OFP–$SiO_2$ colloidal solution (Figure 4a), and the $^{19}F$ MRI signal intensity was proportional to $C_F$ (Figure 4b). Alternatively, the photothermal imaging capability of the nanoprobes was also evaluated. Under the irradiation of 808 nm with a power density of 0.5 W/cm$^2$, the temperature of the $Cu_{1.75}S$–$^{19}F$@OFP–$SiO_2$ colloids increased rapidly (Figure S6). In addition, the more dosage of the colloids, the quicker and higher the temperature increased (Figure S6b). To be specific, with 80 $\mu$g/mL of nanoprobes, the temperature would increase from 29 to 68 °C within 3 min (Figure S6b). The corresponding photothermal images at different time intervals under different concentrations were also recorded (Figure S6a). All of the results clearly indicated that these multifunctional nanoprobes are applicable for $^{19}F$ MRI, photothermal imaging, and photothermal ablation.

### *In Vivo* $^{19}F$ MRI and Photothermal Therapy Tests

Encouraged by the aforementioned promising results, we explored the possibility of using these nanoprobes for *in vivo* studies. As shown in Figure 5a, $^1H$ MRI was carried out to show the anatomic structure of the mouse and the profile of the tumor; however, it is hard to clearly delineate the boundary of the tumor from the surrounding normal tissues. As expected, a distinct difference can be observed in $^{19}F$ MR images before and after administration of $Cu_{1.75}S$–$^{19}F$@OFP–$SiO_2$ NPs (Figure 5b,c). Additionally, photothermal properties were also examined by irradiation of tumor xenografted mice with NIR light for different time intervals. The tumor site displays much brighter photothermal images compared with the surrounding medium (Figure 5d). The temperature at the tumor sites quickly increased from 34.5 to 57.4 °C within 10 min (Figure 5e), which is highly desirable for photothermal ablation. After photothermal treatment, the changes of tumors with an initial volume of ~256 mm$^3$ were tracked by $^1H$ MRI. As shown in Figure 5f,g, the tumors have completely disappeared after 2 weeks. In the meantime, the body weight of the mice slightly increased (Figure 5g). As a control, the tumor injected with PBS solution and $Cu_{1.75}S$–$^{19}F$@OFP–$SiO_2$ colloids was further treated with and without 808 nm light, respectively. As shown in Figure S7a, after injection with $Cu_{1.75}S$–$^{19}F$@OFP–$SiO_2$ NPs but without laser irradiation, the tumor would grow day by day. If the $Cu_{1.75}S$–$^{19}F$@OFP–$SiO_2$ NPs were replaced with PBS and then irradiated with 808 nm light (1.0 W/cm$^2$) for 10 min, the tumor size decreased in the next day and then increased step-by-step. Meanwhile, the body weight of mice decreased with the growth of the tumor (Figure S7b). In addition, from Figure S7a, it is clear that although the initial tumor size is smaller than that shown in Figure 5g, it still grew gradually if no NIR irradiation or photothermal agent was introduced. These observations demonstrate that the $Cu_{1.75}S$–$^{19}F$@OFP–$SiO_2$ NPs hold great potentials as multifunctional platforms for diagnosis and therapy of tumors.

### Generality Tests of This Facile Fabrication Strategy

We also explored the possibility of using this facile nanoprobe fabrication strategy for the preparation of other multifunctional nanoprobes such as ZnS:$Mn^{2+}$ quantum dots (Figure 6a), $NaYF_4$:$Yb^{3+}$/$Er^{3+}$ upconversion luminescence nanoparticles (Figure 6b), and $Ag_2S$ near-infrared fluorescence quantum dots (Figure 6c). As shown in the TEM images, all three kinds of hydrophobic nanoparticles were successfully encapsulated in the hydrophilic micelle with one particle per micelle, and no aggregation was observed. Meanwhile, the $^{19}F$ NMR spectra of these nanoprobes demonstrated a symmetric peak at −91.85 ppm, which is very similar to that of the as-prepared $Cu_{1.75}S$–$^{19}F$@OFP–$SiO_2$ nanoprobes despite the slight influence of the paramagnetic element. All the results indicate that our nanoprobe fabrication method is a general and facile strategy that can be easily extended to other kinds of multifunctional nanoprobes.

## CONCLUSIONS

In conclusion, we have presented the $Cu_{1.75}S$–$^{19}F$@OFP–$SiO_2$ nanoprobes with strong $^{19}F$ MRI signals and small DLS size, which can be applied as $^{19}F$ MRI and photothermal imaging contrast agents and for photothermal therapy. Preliminary experiments show that the multimodal nanoprobes are highly biocompatible under the conditions tested, which can be attributed to encapsulation of the $Cu_{1.75}S$ core within the biocompatible poly(amino acid) and silica shell. We believe that this new class of multifunctional agents creates the opportunity to significantly improve localized therapy using focused photothermal effects under sensitive $^{19}F$ MR imaging guidance. The targeted imaging study by grafting specific biological moieties such as peptides is underway. This versatile fabrication strategy can be readily extended to other single-particle nanoprobes for ablation and multimodal imaging such as MRI fluorescence and MRI computer tomography.

## EXPERIMENTAL SECTION

### Chemicals and Reagents

General chemicals were of the highest grade available (at least analytical grade) and used as received without further purification. Absolute ethanol, methanol, chloroform, dimethylformamide (DMF), NaOH, $NaH_2PO_4{\cdot}2H_2O$, $Na_2HPO_4{\cdot}12H_2O$, and $Cu(NO_3)_2{\cdot}3H_2O$ were supplied by Beijing Chemical Reagent Company. Polyvinylpyrrolidone ($M_w$ ~ 10 000) was purchased from Aldrich. Oleylamine was obtained from Acros. mPEG-SH ($M_w$ ~ 5000) was purchased from Tianjin Golden Biotechnology Co. Ltd. TMOS and PFCE were obtained from Fluorochem. Ltd. Polysuccinimide ($M_w$ ~ 6000) was supplied by Shijiazhuang Desai Chemical Company (China). Dibutyl dithiocarbamate was supplied by Pacific Ocean United (Beijing) Petro-Chemical Co. Ltd. Diatomite was purchased from Tianjin Fuchen Chemical Reagents Factory. Ultrapure water was made by a Milli-Q water purification system from Millipore (Bedford, MA, USA).

### Characterization

$^{19}F$ NMR spectra were measured on a Bruker Avance-III 400 instrument at 376 MHz. The chemical shift is relative to neat $CFCl_3$ (external reference). FTIR spectra were acquired on a

Nicolet 670 FTIR spectrophotometer. XRD patterns were measured on a Rigaku SmartLab X-ray diffractometer using Cu K$\alpha$ radiation ($\lambda$ = 1.5418 Å) over the range of 2$\theta$ from 5 to 90°. TEM images were acquired by using a JEOL JEM-1200EX (200 kV). DLS particle size analysis was carried out using a Zetasizer Nano-ZS90 zeta and size analyzer from Malvern. UV–vis–NIR absorption spectra were acquired on a UV-3600 spectrophotometer (Shimadzu) equipped with a plotter unit over the range of wavelength from 300 to 3300 nm.

### Preparation of $Cu_{1.75}S$ Nanoparticles

The hydrophobic $Cu_{1.75}S$ nanoparticles with strong near-infrared localized surface plasmon resonance absorption (Figure S8) were prepared according to our previously developed strategy with some modification.[32] Briefly, copper nitrate ($Cu(NO_3)_2{\cdot}3H_2O$, 242 mg, 1.0 mmol) and dibutyl dithiocarbamate (200 mg) were dissolved in 2 mL of ethanol under ultrasonication until the mixture became a transparent solution. Oleylamine (20 mL) and 1-octadecene (30 mL) were added into a three-necked flask with nitrogen ($N_2$) purging for 15 min. Thereafter, the mixture was heated to 205 °C with continuous stirring, and the transparent solution prepared above was then injected into the flask quickly and the temperature kept at 190 °C for 15 min. After being cooled to room temperature, the $Cu_{1.75}S$ NPs were collected by precipitation with ethanol, followed by centrifugation for 10 min at the speed of 8000 rpm for two times (the solid was redispersed in cyclohexane before the second time). The final product was dispersed in chloroform (5.0 mL) and stored at 4 °C for further use.

### Preparation of OFP

The OFP was synthesized according to our previous method with minor alteration.[43] Polysuccinimide (1.6 g) was dissolved in 32 mL of DMF, and the mixture was stirred for 5 h at 90 °C. Then, oleylamine (1.63 mL) was added, and stirring continued for another 5 h at 100 °C. After being cooled to room temperature, the solid product was harvested by precipitation with methanol, followed by centrifugation at a speed of 7000 rpm for 5 min. The final product (OFP) was dispersed in chloroform (8.0 mL).

### Preparation of Water-Dispersible $Cu_{1.75}S$–$^{19}F$@OFP–$SiO_2$

$Cu_{1.75}S$ NPs (4.0 mg), PVP (2.0 mg), mPEG-SH (3.0 mg), TMOS (25 $\mu$L, 22.13 mg), PFCE (28 mg), and OFP (40 mg) were dissolved in 1.0 mL of $CHCl_3$. Then, the mixture was added into NaOH aqueous solution (0.01 M, 10 mL) with ultrasonication treatment (300 W for 6 min, pulsed working as 3 s “on” and 3 s “off”). After the resultant mixture solution changed into an emulsion, the $CHCl_3$ was removed at ambient temperature to get a clear solution which was then centrifuged with water three times at a speed of 18 000 rpm for 15 min. Along with the formation of $Cu_{1.75}S$–$^{19}F$@OFP–$SiO_2$, the surface of $Cu_{1.75}S$ NPs was coated with a silica and OFP–$COO^-$ layer (the lactam rings were hydrolyzed to carboxylic groups under alkaline condition), which makes the entire nanocomposite water-dispersible. The final product was dispersed in PBS buffer (0.02 M, 1.0 mL) for further imaging experiments. Similarly, for comparison, $Cu_{1.75}S$–$^{19}F$@OFP NPs, $Cu_{1.75}S$–$^{19}F$@OFP–thiol-PEG NPs, and $Cu_{1.75}S$–$^{19}F$@OFP–PVP NPs without $SiO_2$ were also prepared with the above-mentioned method for $Cu_{1.75}S$–$^{19}F$@OFP–$SiO_2$ NPs.

### $^{19}$F NMR Measurements

Water-dispersible nanocomposites ($Cu_{1.75}S$–$^{19}$F@OFP, $Cu_{1.75}S$–$^{19}$F@OFP–$SiO_2$, and $Cu_{1.75}S$–$^{19}$F@OFP–thiol-PEG) were prepared in water by using a coaxially $D_2O$-filled capillary tube for locking the field. The external standard $CF_3COONa$ was also dissolved in water with $D_2O$ in a coaxial capillary tube for the field locking. All of the $^{19}$F magnetic resonance spectra were recorded by utilizing a "single-pulse" sequence (a Bruker "zg" sequence) without decoupling of $^1$H. The major parameters were set as follows: the spectral width was 89 286 Hz; the size of FID was 64 k; the acquisition time was 0.367 s; the number of accumulation was 128; the relaxation delay was 2 s; and the pulse angle was 45°.

### MRI Measurements

All the MRI images were taken on a 9.4 T Bruker BioSpec MRI system. The RARE-$T_2$ (rapid acquisition with refocused echoes) method was employed for $^1$H MRI. The parameters for $^1$H MRI were set as follows: the number of accumulations was 2, and the repetition time (TR) and the effective time (TE) were 2500 and 3.3 ms, respectively. The field of view was set as 40 mm × 40 mm, and the slice thickness was 1 mm. The matrix size was 256 × 256. Correspondingly, the FLASH method was applied for $^{19}$F MRI, and the parameters were as follows: the number of accumulations was 64, and TR and TE were 800 and 1.3 ms, respectively. The field of view was 40 mm × 40 mm with the slice thickness of 10 mm. The matrix size was 32 × 32, and the total accumulation time was approximately 27 min.

### Cell Viability

The cytotoxicity of the as-prepared imaging contrast agents, such as $Cu_{1.75}S$–$^{19}$F@OFP, $Cu_{1.75}S$–$^{19}$F@OFP–$SiO_2$, $Cu_{1.75}S$–$^{19}$F@OFP–thiol-PEG, and $Cu_{1.75}S$–$^{19}$F@PVP, was evaluated *via* the methyl thiazolyltetrazolium (MTT) assay against the cultured HeLa cell lines according to previous reports.[33,43,44] Briefly, HeLa cells (~5 × $10^4$ cells/well) were seeded in a 96-well microtiter plate, and then different amounts of the aforementioned hydrophilic nanocomposites (calculated with $C_{NPs}$ from 0 to 400 $\mu$g/mL) were added and cultured at 37 °C for 24 or 48 h under 5% $CO_2$ and a 95% relative humidity atmosphere, respectively. Thereafter, 10 $\mu$L of sterile-filtered MTT stock solution in PBS (4.0 mg/mL) was added to each well. The 96- well microtiter plate was incubated at 37 °C for another 3 h. The absorbance of the soluble colored formazan produced by cellular reduction of MTT (the reduction takes place only when the mitochondrial reductases are active, *i.e.*, the cells are viable) in each well was measured at 490 nm using an ELISA plate reader (F50, TECAN). The larger viable cell number results in the increase in the amount of MTT formazan and the increase in absorbance.

### Tumor Model and *In Vivo* Experimental Procedure for MRI and Photothermal Therapy

Animal experiments were performed using female mice (Balb/c) between 4 and 5 weeks old (18–21 g body weight). The tumor-bearing mice were prepared. First, the 4T1 cells were centrifuged at 1000 rpm for 5 min at 4 °C and resuspended in PBS (pH 7.4) to a final concentration of 1 × $10^7$ cells/mL. Then, approximately 1 × $10^6$ 4T1 cells were subcutaneously inoculated on the right leg of mice and allowed to grow for 2 weeks, and

typically, a solid tumor formed during this period. Prior to imaging experiments, the mice bearing tumors (size of the tumor was around 250 $mm^3$) were administered 100 $\mu$L of $Cu_{1.75}S$–$^{19}F$@OFP–$SiO_2$ solution (11 mg/mL in PBS) through intratumor injection. MRI measurements of live mice were carried out using 100 $\mu$L of 7% chloral hydrate through intraperitoneal injection for anesthetizing.

Photothermal imaging and therapy experiments were performed on an 808 nm laser instrument (STL808CF-10W). For the *in vitro* test for the evaluation of the photothermal properties of the as-prepared $Cu_{1.75}S$–$^{19}F$@OFP–$SiO_2$ NPs, different concentrations were investigated under 0.5 W/$cm^2$ power density of the irradiation for 10 min. For the *in vivo* measurements, after administration of 100 $\mu$L of $Cu_{1.75}S$–$^{19}F$@OFP–$SiO_2$ solution, the tumor-bearing mice were exposed to an 808 nm laser irradiation with power density of 1.0 W/$cm^2$ for 10 min under isoflurane. Then, the changes of the tumor volume and the body weight of the mice were monitored at different days (1, 3, 7, and 14) for PTT.

## Supplementary Material

Refer to Web version on PubMed Central for supplementary material.

## Acknowledgments

This research was supported in part by the National Natural Science Foundation of China (Grant Nos. 21475007, 21275015, and 21271030), the State Key Project of Fundamental Research of China (Grant No. 2011CB932403), and the intramural research program of the National Institute of Biomedical Imaging and Bioengineering. We also thank the support from the “Innovation and Promotion Project of Beijing University of Chemical Technology”, the “Public Hatching Platform for Recruited Talents of Beijing University of Chemical Technology”, the “High-Level Faculty Program of Beijing University of Chemical Technology (buctrc201507, buctrc201325)”, and BUCT Fund for Disciplines Construction and Development (Project No. XK1526).

## References

1. Chen H, Viel S, Ziarelli F, Peng L. F-19 NMR: A Valuable Tool for Studying Biological Events. Chem Soc Rev. 2013; 42:7971–7982. [PubMed: 23864138]
2. Takaoka Y, Sakamoto T, Tsukiji S, Narazaki M, Matsuda T, Tochio H, Shirakawa M, Hamachi I. Self-Assembling Nanoprobes that Display off/on F-19 Nuclear Magnetic Resonance Signals for Protein Detection and Imaging. Nat Chem. 2009; 1:557–561. [PubMed: 21378937]
3. Yamaguchi K, Ueki R, Nonaka H, Sugihara F, Matsuda T, Sando S. Design of Chemical Shift-Switching F-19 Magnetic Resonance Imaging Probe for Specific Detection of Human Monoamine Oxidase A. J Am Chem Soc. 2011; 133:14208–14211. [PubMed: 21851116]
4. Srinivas M, Heerschap A, Ahrens ET, Figdor CG, de Vries IJM. F-19 MRI for Quantitative in Vivo Cell Tracking. Trends Biotechnol. 2010; 28:363–370. [PubMed: 20427096]
5. Tirotta I, Dichiarante V, Pigliacelli C, Cavallo G, Terraneo G, Bombelli FB, Metrangolo P, Resnati G. $^{19}F$ Magnetic Resonance Imaging (MRI): From Design of Materials to Clinical Applications. Chem Rev. 2015; 115:1106–1129. [PubMed: 25329814]
6. Ahrens ET, Flores R, Xu HY, Morel PA. In Vivo Imaging Platform for Tracking Immunotherapeutic Cells. Nat Biotechnol. 2005; 23:983–987. [PubMed: 16041364]
7. George C, Chandrakumar N. Chemical-Shift-Resolved F-19 NMR Spectroscopy between 13.5 and 135 MHz: Overhauser-DNP-Enhanced Diagonal Suppressed Correlation Spectroscopy. Angew Chem, Int Ed. 2014; 53:8441–8444.
8. Boehm-Sturm P, Mengler L, Wecker S, Hoehn M, Kallur T. In Vivo Tracking of Human Neural Stem Cells with F-19 Magnetic Resonance Imaging. PLoS One. 2011; 6:e29040. [PubMed: 22216163]

9. Langereis S, Keupp J, van Velthoven JLJ, de Roos IHC, Burdinski D, Pikkemaat JA, Grull H. A Temperature-Sensitive Liposomal H-1 CEST and F-19 Contrast Agent for MR Image-Guided Drug Delivery. J Am Chem Soc. 2009; 131:1380–1381. [PubMed: 19173663]

10. Takaoka Y, Kiminami K, Mizusawa K, Matsuo K, Narazaki M, Matsuda T, Hamachi I. Systematic Study of Protein Detection Mechanism of Self-Assembling F-19 NMR/MRI Nanoprobes toward Rational Design and Improved Sensitivity. J Am Chem Soc. 2011; 133:11725–11731. [PubMed: 21699190]

11. Mizukami S, Takikawa R, Sugihara F, Hori Y, Tochio H, Walchli M, Shirakawa M, Kikuchi K. Paramagnetic Relaxation-Based F-19 MRI Probe to Detect Protease Activity. J Am Chem Soc. 2008; 130:794–795. [PubMed: 18154336]

12. Matsushita H, Mizukami S, Sugihara F, Nakanishi Y, Yoshioka Y, Kikuchi K. Multifunctional Core-Shell Silica Nanoparticles for Highly Sensitive F-19 Magnetic Resonance Imaging. Angew Chem, Int Ed. 2014; 53:1008–1011.

13. Yanagisawa D, Taguchi H, Ibrahim NF, Morikawa S, Shiino A, Inubushi T, Hirao K, Shirai N, Sogabe T, Tooyama I. Preferred Features of a Fluorine-19 MRI Probe for Amyloid Detection in the Brain. J Alzheimers Dis. 2014; 39:617–631. [PubMed: 24246421]

14. Janjic JM, Srinivas M, Kadayakkara DKK, Ahrens ET. Self-Delivering Nanoemulsions for Dual Fluorine-19 MRI and Fluorescence Detection. J Am Chem Soc. 2008; 130:2832–2841. [PubMed: 18266363]

15. Patrick MJ, Janjic JM, Teng HB, O'Hear MR, Brown CW, Stokum JA, Schmidt BF, Ahrens ET, Waggoner AS. Intracellular pH Measurements Using Perfluorocarbon Nanoemulsions. J Am Chem Soc. 2013; 135:18445–18457. [PubMed: 24266634]

16. Hu LZ, Chen JJ, Yang XX, Caruthers SD, Lanza GM, Wickline SA. Rapid Quantification of Oxygen Tension in Blood Flow with A Fluorine Nanoparticle Reporter and A Novel Blood Flow-Enhanced-Saturation-Recovery Sequence. Magn Reson Med. 2013; 70:176–183. [PubMed: 22915328]

17. O'Hanlon CE, Amede KG, O'Hear MR, Janjic JM. NIR-Labeled Perfluoropolyether Nanoemulsions for Drug Delivery and Imaging. J Fluorine Chem. 2012; 137:27–33.

18. Thurecht KJ, Blakey I, Peng H, Squires O, Hsu S, Alexander C, Whittaker AK. Functional Hyperbranched Polymers: Toward Targeted in Vivo F-19 Magnetic Resonance Imaging Using Designed Macromolecules. J Am Chem Soc. 2010; 132:5336–5337. [PubMed: 20345132]

19. Huang XN, Huang G, Zhang SR, Sagiyama K, Togao O, Ma XP, Wang YG, Li Y, Soesbe TC, Sumer BD, Takahashi M, Sherry AD, Gao JM. Multi-Chromatic pH-Activatable F-19-MRI Nanoprobes with Binary ON/OFF pH Transitions and Chemical-Shift Barcodes. Angew Chem, Int Ed. 2013; 52:8074–8078.

20. Romero-Aburto R, Narayanan TN, Nagaoka Y, Hasumura T, Mitcham TM, Fukuda T, Cox PJ, Bouchard RR, Maekawa T, Kumar DS, Torti SV, Mani SA, Ajayan PM. Fluorinated Graphene Oxide; a New Multimodal Material for Biological Applications. Adv Mater. 2013; 25:5632–5637. [PubMed: 24038195]

21. Hu YH. The First Magnetic-Nanoparticle-Free Carbon-Based Contrast Agent of Magnetic-Resonance Imaging-Fluorinated Graphene Oxide. Small. 2014; 10:1451–1452. [PubMed: 24376224]

22. Boccalon M, Franchi P, Lucarini M, Delgado JJ, Sousa F, Stellacci F, Zucca I, Scotti A, Spreafico R, Pengo P, Pasquato L. Gold Nanoparticles Protected by Fluorinated Ligands for F-19 MRI. Chem Commun. 2013; 49:8794–8796.

23. Chen SZ, Yang YQ, Li HD, Zhou X, Liu ML. pH-Triggered Au-Fluorescent Mesoporous Silica Nanoparticles for F-19 MR/Fluorescent Multimodal Cancer Cellular Imaging. Chem Commun. 2014; 50:283–285.

24. Wang Z, Yue XY, Wang Y, Qian CQ, Huang P, Lizak M, Niu G, Wang F, Rong PF, Kiesewetter DO, Ma Y, Chen XY. A Symmetrical Fluorous Dendron-Cyanine Dye-Conjugated Bimodal Nanoprobe for Quantitative F-19 MRI and NIR Fluorescence Bioimaging. Adv Healthcare Mater. 2014; 3:1326–1333.

25. Rolfe BE, Blakey I, Squires O, Peng H, Boase NRB, Alexander C, Parsons PG, Boyle GM, Whittaker AK, Thurecht KJ. Multimodal Polymer Nanoparticles with Combined F-19 Magnetic

Resonance and Optical Detection for Tunable, Targeted, Multimodal Imaging in Vivo. J Am Chem Soc. 2014; 136:2413–2419. [PubMed: 24437730]

26. Mizukami S, Takikawa R, Sugihara F, Shirakawa M, Kikuchi K. Dual-Function Probe to Detect Protease Activity for Fluorescence Measurement and F-19 MRI. Angew Chem, Int Ed. 2009; 48:3641–3643.
27. Lim YT, Noh YW, Cho JH, Han JH, Choi BS, Kwon J, Hong KS, Gokarna A, Cho YH, Chung BH. Multiplexed Imaging of Therapeutic Cells with Multispectrally Encoded Magneto-fluorescent Nanocomposite Emulsions. J Am Chem Soc. 2009; 131:17145–17154. [PubMed: 19894710]
28. Liang C, Diao S, Wang C, Gong H, Liu T, Hong GS, Shi XZ, Dai HJ, Liu Z. Tumor Metastasis Inhibition by Imaging-Guided Photothermal Therapy with Single-Walled Carbon Nanotubes. Adv Mater. 2014; 26:5646–5652. [PubMed: 24924258]
29. Song XJ, Gong H, Yin SN, Cheng L, Wang C, Li ZW, Li YG, Wang XY, Liu G, Liu Z. Ultra-Small Iron Oxide Doped Polypyrrole Nanoparticles for In Vivo Multimodal Imaging Guided Photothermal Therapy. Adv Funct Mater. 2014; 24:1194–1201.
30. Cheng L, Yang K, Li YG, Chen JH, Wang C, Shao MW, Lee ST, Liu Z. Facile Preparation of Multifunctional Upconversion Nanoprobes for Multimodal Imaging and Dual-Targeted Photothermal Therapy. Angew Chem, Int Ed. 2011; 50:7385–7390.
31. Huang S, Liu J, He Q, Chen HL, Cui JB, Xu SY, Zhao YL, Chen CY, Wang LY. Smart $Cu_{1.75}S$ Nanocapsules with High and Stable Photothermal Efficiency for NIR Photo-Triggered Drug Release. Nano Res. 2015; 8:4038–4047.
32. Cui JB, Xu SY, Guo C, Jiang R, James TD, Wang LY. Highly Efficient Photothermal Semiconductor Nanocomposites for Photothermal Imaging of Latent Fingerprints. Anal Chem. 2015; 87:11592–11598. [PubMed: 26494177]
33. Huang S, Peng S, Li YB, Cui JB, Chen HL, Wang LY. Development of NIR-II Fluorescence Image-Guided and pH-Responsive Nanocapsules for Cocktail Drug Delivery. Nano Res. 2015; 8:1932–1943.
34. Roper DK, Ahn W, Hoepfner M. Microscale Heat Transfer Transduced by Surface Plasmon Resonant Gold Nanoparticles. J Phys Chem C. 2007; 111:3636–3641.
35. Chou SS, Kaehr B, Kim J, Foley BM, De M, Hopkins PE, Huang J, Brinker CJ, Dravid VP. Chemically Exfoliated $MoS_2$ as Near-Infrared Photothermal Agents. Angew Chem, Int Ed. 2013; 52:4160–4164.
36. Hessel CM, Pattani VP, Rasch M, Panthani MG, Koo B, Tunnell JW, Korgel BA. Copper Selenide Nanocrystals for Photothermal Therapy. Nano Lett. 2011; 11:2560–2566. [PubMed: 21553924]
37. Liu HY, Chen D, Li LL, Liu TL, Tan LF, Wu XL, Tang FQ. Multifunctional Gold Nanoshells on Silica Nanorattles: A Platform for the Combination of Photothermal Therapy and Chemotherapy with Low Systemic Toxicity. Angew Chem, Int Ed. 2011; 50:891–895.
38. Lv RC, Yang PP, He F, Gai SL, Yang GX, Lin J. Hollow Structured $Y_2O_3$:Yb/Er-CuxS Nanospheres with Controllable Size for Simultaneous Chemo/Photothermal Therapy and Bioimaging. Chem Mater. 2015; 27:483–496.
39. Tian QW, Hu JQ, Zhu YH, Zou RJ, Chen ZG, Yang SP, Li RW, Su QQ, Han Y, Liu XG. Sub-10 nm $Fe_3O_4$@$Cu_{2-x}S$ Core-Shell Nanoparticles for Dual-Modal Imaging and Photothermal Therapy. J Am Chem Soc. 2013; 135:8571–8577. [PubMed: 23687972]
40. Zhang ZJ, Wang J, Nie X, Wen T, Ji YL, Wu XC, Zhao YL, Chen CY. Near Infrared Laser-Induced Targeted Cancer Therapy Using Thermoresponsive Polymer Encapsulated Gold Nanorods. J Am Chem Soc. 2014; 136:7317–7326. [PubMed: 24773323]
41. Cheng L, Yang K, Chen Q, Liu Z. Organic Stealth Nanoparticles for Highly Effective in Vivo Near-Infrared Photothermal Therapy of Cancer. ACS Nano. 2012; 6:5605–5613. [PubMed: 22616847]
42. Tian QW, Jiang FR, Zou RJ, Liu Q, Chen ZG, Zhu MF, Yang SP, Wang JL, Wang JH, Hu JQ. Hydrophilic $Cu_9S_5$ Nanocrystals: A Photothermal Agent with a 25. 7% Heat Conversion Efficiency for Photothermal Ablation of Cancer Cells in Vivo. ACS Nano. 2011; 5:9761–9771. [PubMed: 22059851]

43. Huang S, Bai M, Wang LY. General and Facile Surface Functionalization of Hydrophobic Nanocrystals with Poly(amino acid) for Cell Luminescence Imaging. Sci Rep. 2013; 3:2023–2027. [PubMed: 23778122]

44. Deng ML, Wang LY. Unexpected Luminescence Enhancement of Upconverting Nanocrystals by Cation Exchange with Well Retained Small Particle Size. Nano Res. 2014; 7:782–793.

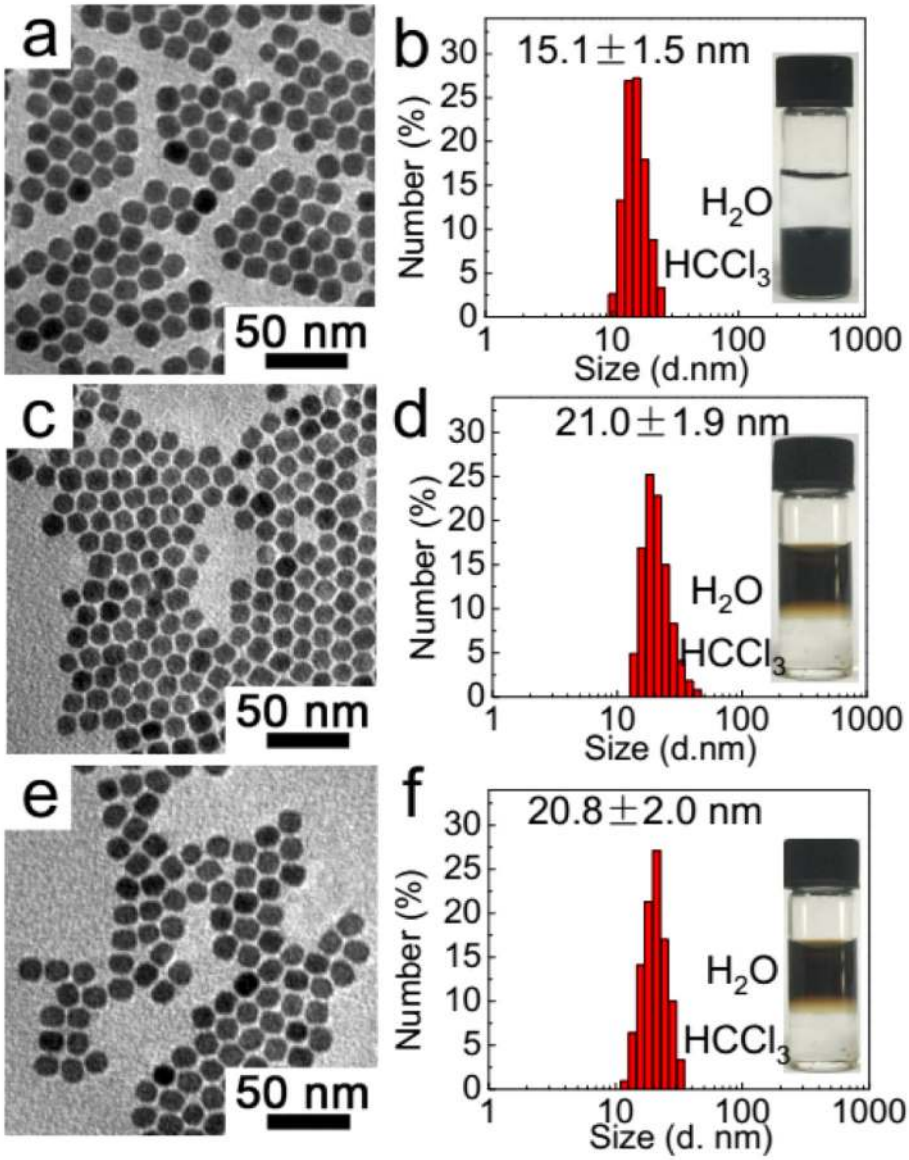


**Figure 1.**

TEM images (a,c,e) and DLS size distribution (b,d,f) of hydrophobic $Cu_{1.75}S$ (a,b), $Cu_{1.75}S$–$^{19}F$@OFP (c,d), and $Cu_{1.75}S$–$^{19}F$@OFP–$SiO_2$ (e,f). Insets of (b,d,e) are the photographs of the nanoparticle colloids before and after surface modification.

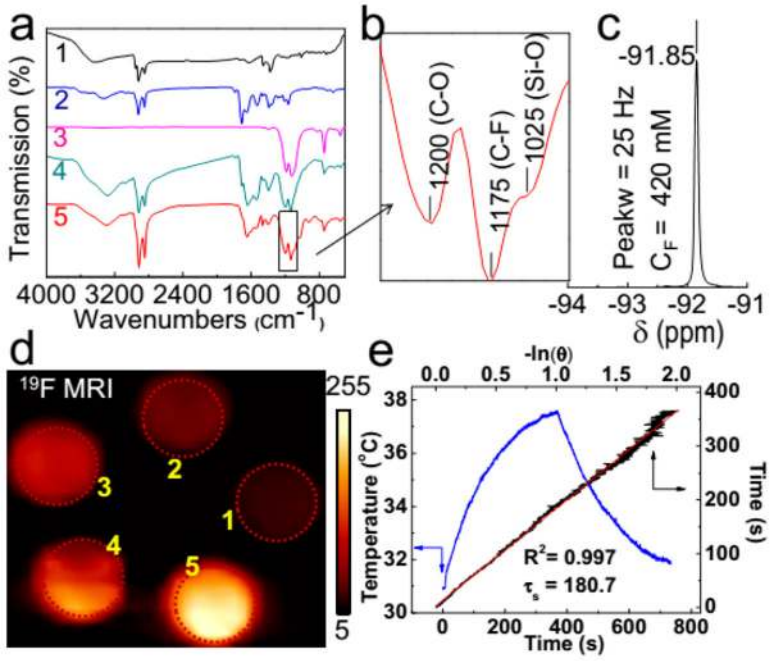


**Figure 2.**

(a) FTIR spectra of hydrophobic $Cu_{1.75}S$ (a1), OFP (a2), PFCE (a3), $Cu_{1.75}S$–$^{19}F$@OFP (a4), and $Cu_{1.75}S$–$^{19}F$@OFP–$SiO_2$ (a5). (b) Magnification of FTIR spectrum in the box of (a5). (c) $^{19}F$ NMR spectrum of $Cu_{1.75}S$–$^{19}F$@OFP–$SiO_2$ aqueous solution (11.0 mg/mL). (d) $^{19}F$ MR images of $Cu_{1.75}S$–$^{19}F$@OFP–$SiO_2$ colloidal solution with various $^{19}F$ concentrations ($C_F$). (1–5): 66.25, 132.5, 265, 397.5, 530 mM. (e) Temperature profile (blue) of $Cu_{1.75}S$ colloids (4 mg/mL) irradiated by 808 nm laser (0.45 W/cm$^2$) for 360 s, followed by natural cooling for calculating the photothermal conversion efficiency ($\eta = 54.13\%$). The linear fitting (red) of time from the cooling period *versus* negative natural logarithm of driving force temperature.

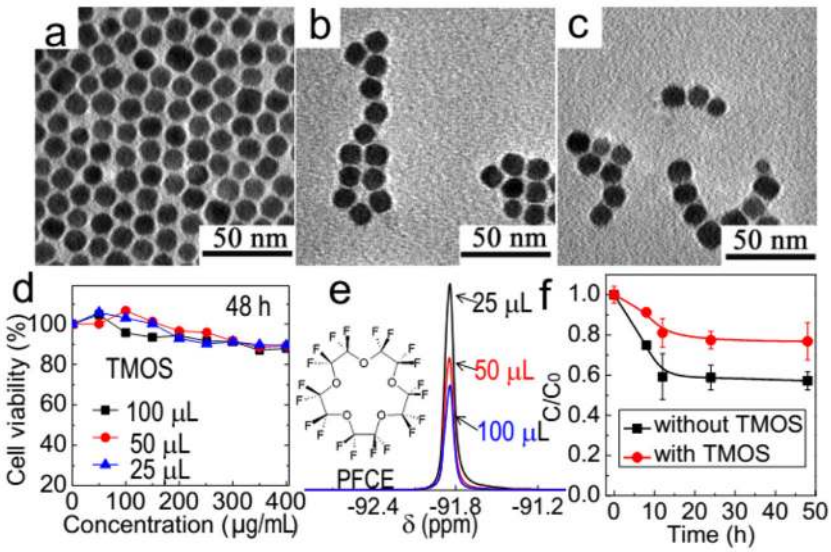


**Figure 3.**

TEM images of $Cu_{1.75}S$–$^{19}F$@OFP–$SiO_2$ NPs prepared with 25 (a), 50 (b), and 100 $\mu$L (c) of TMOS. (d) Cytotoxicity tests of $Cu_{1.75}S$–$^{19}F$@OFP–$SiO_2$ NPs after incubation with HeLa cell lines for 48 h. (e) $^{19}F$ NMR spectra of $Cu_{1.75}S$–$^{19}F$@OFP–$SiO_2$ prepared with different amounts of TMOS. Inset of (e) is the chemical structure of PFCE. (f) Plots for the PFCE leakage tests *via* dialysis. $C$ and $C_0$ represent the fluorine concentration in $Cu_{1.75}S$–$^{19}F$@OFP–$SiO_2$ colloidal solution after and before dialysis in PBS for different time intervals, respectively.

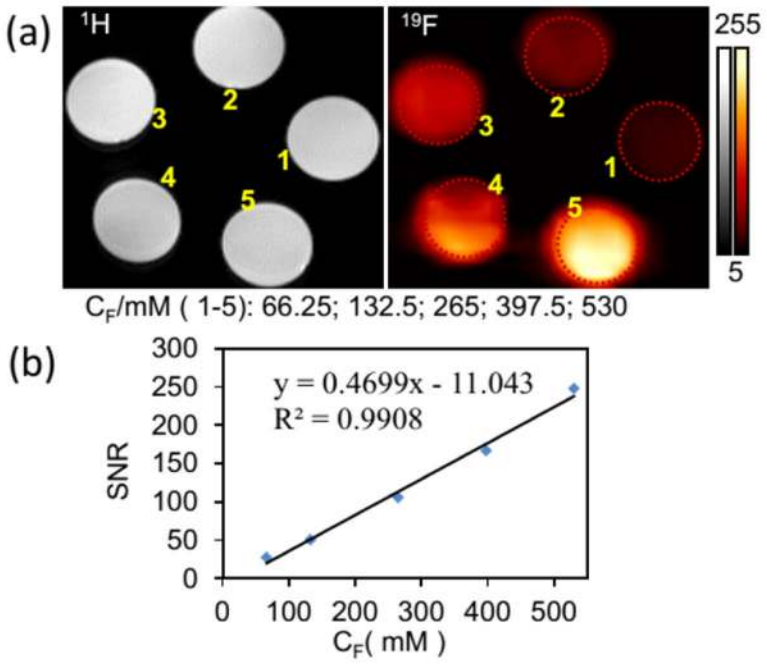


**Figure 4.**

(a) $^{1}$H and $^{19}$F magnetic resonance images of $Cu_{1.75}S$–$^{19}$F@OFP–$SiO_2$ colloidal solution with various $^{19}$F concentrations ($C_F$). (1–5): 66.25, 132.5, 265, 397.5, 530 mM. (b) Plot of the $^{19}$F MRI signal-to-noise ratio (SNR) *versus* $^{19}$F concentration ($C_F$/mM).

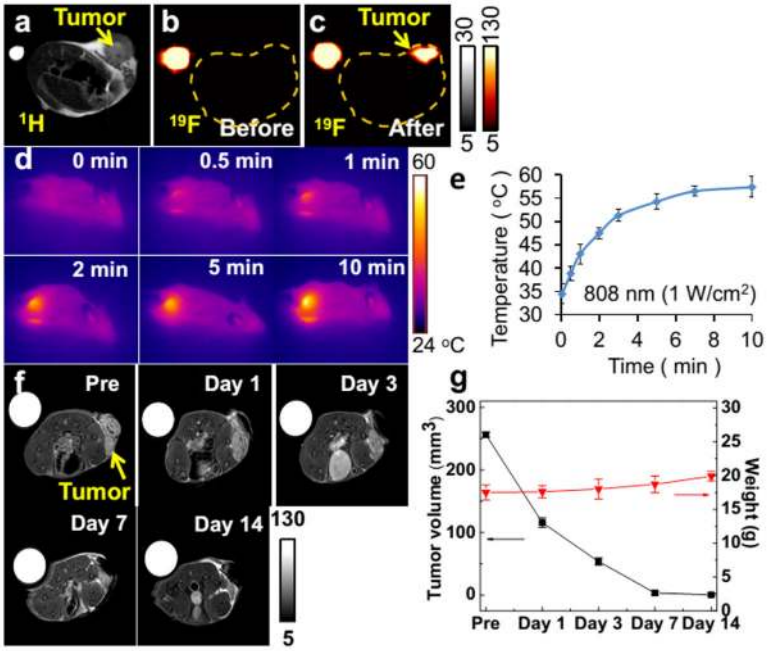


**Figure 5.**

*In vivo* $^{1}$H (a) and $^{19}$F (b,c) MRI of the tumor-bearing mice before (a,b) and after (c) injection of $Cu_{1.75}S$–$^{19}$F@OFP–$SiO_2$ colloidal solution ($C_F$ = 530 mM, 100 $\mu$L). Photothermal images (d) and temperature evolution profile (e) of the tumor under 808 nm laser irradiation (1.0 W/cm$^2$) for 0–10 min. (f) $^{1}$HMRI of the tumor xenografted mice at different days after photothermal treatment. (g) Evolution plots of the tumor size and the mouse body weight after photothermal treatment.

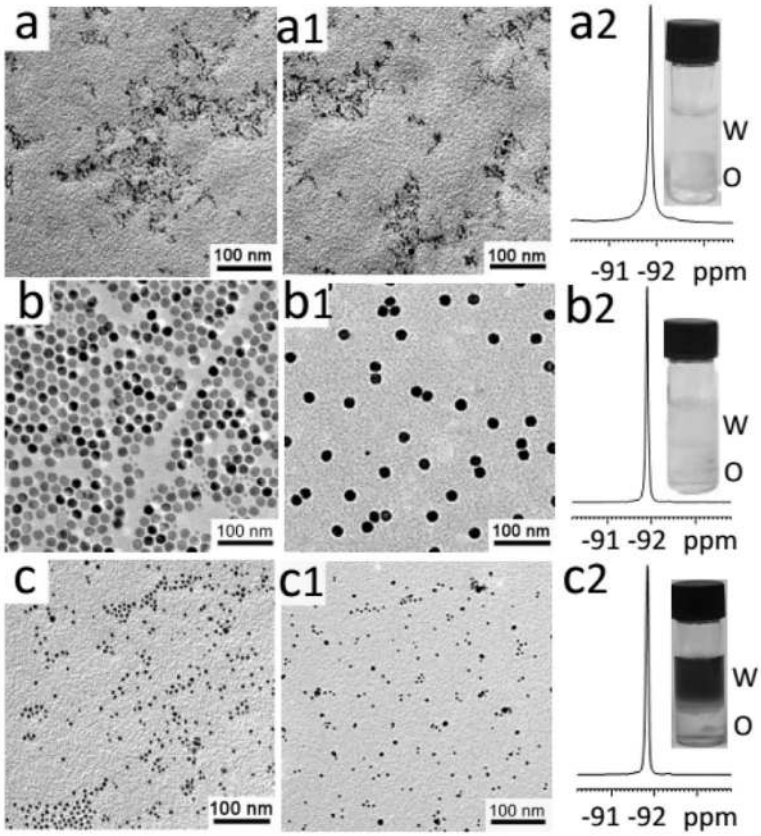


**Figure 6.**

TEM images with low (a–c) and high magnification (a1–c1) and $^{19}$FNMRspectra (a2–c2) of ZnS:$Mn^{2+}$ (a–a2), $NaYF_4$:$Yb^{3+}$/$Er^{3+}$ (b–b2), and $Ag_2S$ (c–c2), respectively.

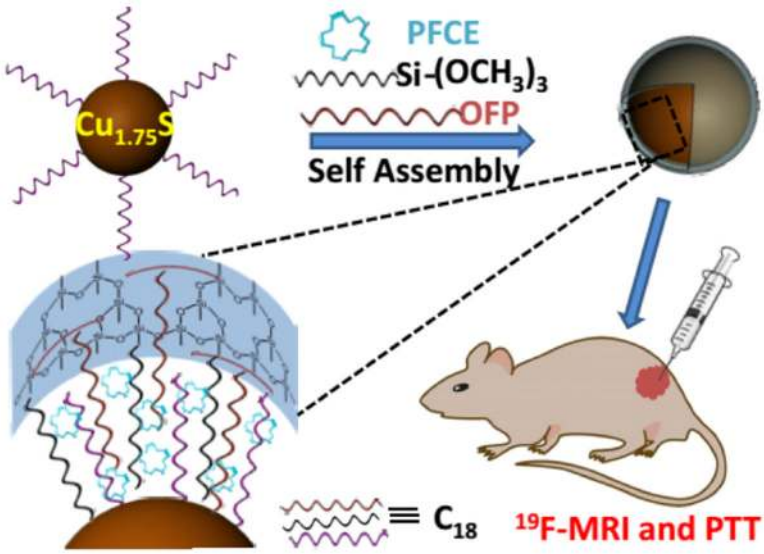


**Scheme 1.**

Illustration Scheme for the Fabrication and Bioapplications of a Multifunctional $Cu_{1.75}S$–$^{19}F$@OFP–$SiO_2$ Nanoprobe, Including $^{19}F$ MRI, PTI, and PTT